CHAPTER 5

Roles of surface and bulk states in magnetotransport properties in antiferromagnetically ordered $Bi_{1.9}Dy_{0.1}Te_3$ topological insulator

Chapter 5

5.1 Introduction

Topological insulators (TIs) have attracted much interest for many exciting physical phenomena like quantum anomalous Hall effect (QAHE), Majorana Fermions, magnetic monopoles and with great possibilities of application in spintronics and quantum computing [1], [25], [112]–[115]. Magnetic TIs provide a route to study the correlation between magnetism and topological surface states (TSS). Moreover, finding the anomalous Hall effect [116] in topological states of matter is highly interesting. In fact, transition metal doped TIs have shown QAHE with long-range ferromagnetic ordering which are suitable source materials for spintronic applications [115]–[117]. Recently, in antiferromagnetic GdPtBi [117], whose electronic structure is similar to the topologically insulating HgTe, the existence of the anomalous Hall Effect has also been reported. Antiferromagnetic TIs have been extensively studied due to the application in spintronics and to decrease the critical current density [118]. It was theoretically predicted that antiferromagnetic ordering does not always destroy TSS. It locally breaks time reversal symmetry (TRS) but maintains global TRS in combination with the translation symmetry. Therefore, the antiferromagnetic order can coexist with TSS [119]–[121].

Recently, rare-earth ion doped topological insulators have drawn much attention [122], [123] as when Bi site is doped via trivalent rare earth elements such as, Gd, and Dy, no additional charge carriers are generated and only magnetic moments are added to the system. In general, rare earth ions have well-shielded 4*f* shell with a large moment and they behave like isolated magnetic impurities in the system. Thus, a doped system should remain paramagnetic. Despite the fact, rare earth doped systems show various magnetic properties which are usually unexpected and complex [124], [125]. Studies on magnetically doped 3D

topological insulators reveal that the gap opening at the Dirac point increases with magnetic moment [30]. Therefore, the highest magnetic moment of Dy (10.65 μ_B) has attracted more attention to explore the effect of magnetic impurity on topological properties. However, some controversial reports are available on Dy-doped Bi_2Te_3 [122], [126], which suggests that further study is needed on the Dy-doped Bi_2Te_3 system. Harrison *et al.* reported a paramagnetic state in Dy-doped Bi_2Te_3 thin films. In their study, fitted magnetic susceptibility data with Curie-Weiss law showed a negative Curie-Weiss temperature (T_C = −1.2 K) and suggested the possibility of an antiferromagnetic phase [126]. In another report by the same group, they found a gap opening at the Dirac point due to Dy doping (but not by Ho, Gd doping) indicating a long-range ferromagnetic ordering. However, no sign of long-range ferromagnetic ordering has been observed and the authors attributed the gap opening to disorder effects [122]. L. B. Duffy *et al.* found in their study that Dy-doped Bi_2Te_3 film is neither ferromagnetic nor fully paramagnetic, but displays a complex, short-range, and inhomogeneous magnetic ordering [125]. Furthermore, so far no report is available on the roles of surface and bulk states on the different magnetotransport properties.

By keeping in mind, the controversial reports on the effect of Dy on the Topological insulators and to throw light on the roles of surface and bulk states on the different magnetotransport properties, we have investigated the electronic structure, magnetotransport and magnetic properties of $Bi_{1.9}Dy_{0.1}Te_3$ topological insulator.

5.2 Experimental Details

We have synthesized $Bi_{1.9}Dy_{0.1}Te_3$ single crystals by a two-step melting method [127]. A stoichiometric mixture of high purity Bi (99.999%), Dy (99.999%) and Te (99.999%)

was sealed in a quartz ampoule at a pressure of ~10^{-6} torr. The sealed quartz ampoule was slowly (60 ^{o}C/h) heated up to 950^{o}C and kept there for a period of 24 h. Then it was cooled from 950 ^{o}C to 550 ^{o}C at the rate of 5 ^{o}C/h, annealed for 72 hours, then slowly (60 ^{o}C/h) cooled down to room temperature.

The structural properties of the samples were characterized by X-Ray diffraction (XRD) measurements. Magnetotransport measurements were carried out by the physical properties measurement system (PPMS). Magnetic measurements were performed by quantum design SQUID magnetic properties measurement system (MPMS). Seebeck coefficient (*S*) of the present sample was measured by a homemade setup with the help of a closed-cycle refrigerator (CCR).

High-resolution angle-resolved photoemission spectroscopy (ARPES) measurements have been performed at the Hiroshima Synchrotron Radiation Center (HiSOR), Hiroshima University, Japan with a focused ultraviolet laser beam (photon energy of 6.3 eV, the beam spot size of ~10 μm) equipped with VG Scienta R4000 electron analyzer [103]. Samples were cleaved in-situ (at 30K) in ultrahigh vacuum (~5×10^{-11} torr). A narrow momentum distribution curve (MDC) of 0.003 $Å^{-1}$ is obtained which indicates a low scattering rate of the cleaved surface. Figure 5.1 shows the X-ray diffraction (XRD) pattern and Laue pattern (Inset) of a $Bi_{1.9}Dy_{0.1}Te_3$ single crystal. XRD reflects all diffraction peaks correspond to the (*00l*) family of rhombohedral planes of Bi_2Te_3, with no sign of secondary phases.

5.3 Results and Discussion

5.3.1 Magnetoresistance and Magnetization

The temperature dependent resistivity (ρ_{xx}) as shown in the inset of figure 5.1 shows the metallic nature of the sample. The residual resistivity ratio (RRR), ρ_{xx}(300 K)/ρ_{xx}(2 K)

[ρ_{xx}(300 K) and ρ_{xx}(2 K) are the resistivity values at T = 300 K and 2 K, respectively] is ~59, which is nearly 3 times larger than that reported by Shrestha *et al.* for pure Bi_2Te_3 [21] indicating the very good crystalline quality.

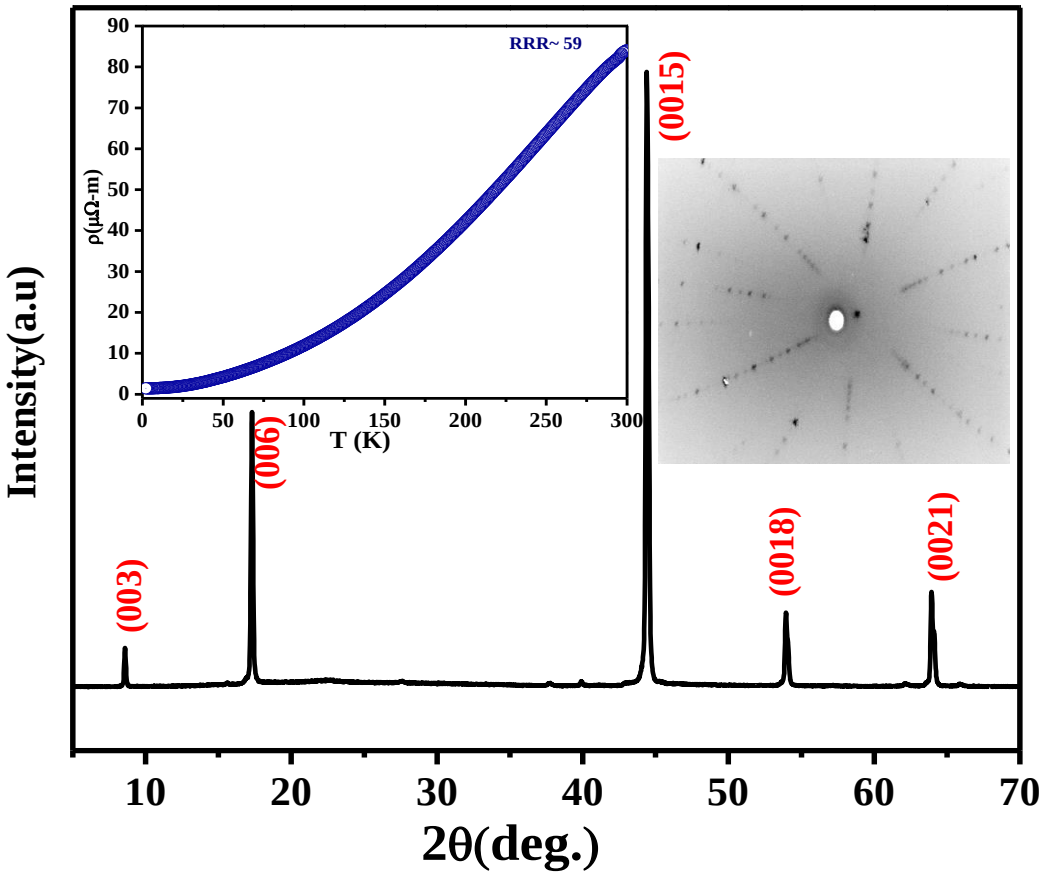

Figure 5.1: (a) X-ray diffraction pattern of single crystalline $Bi_{1.9}Dy_{0.1}Te_3$, Insets: Laue diffraction pattern, and variation of resistivity with temperature for $Bi_{1.9}Dy_{0.1}Te_3$.

Magnetoresistance (MR) measurements were performed at different temperatures as shown in figure 5.2 (a). MR ratio (%) has been defined as $((\rho_{xx}(B) - \rho_{xx}(0)) / \rho_{xx}(0)) \times 100\%$, where $\rho_{xx}(B)$ and $\rho_{xx}(0)$ are the resistivity values under non-zero and zero applied magnetic field (B) [which is normal to the '*ab*' plane] respectively. We obtained a large linear, non-saturated positive MR down to low temperature and up to high magnetic fields. The observed MR value at 2 K and 7 T is as large as 1500%. This MR value is significantly

higher than pure Bi_2Te_3 (MR=540%) as has been reported by Shreshtha *et al.* [128] and is so far the highest reported value for any topological insulator [86], [123]. Moreover, the MR curves display the cusp-like feature at low temperature suggesting the presence of weak anti-localization (WAL) effect [128], [129]. The WAL effect is a manifestation of TSS and mainly comes from the π-Berry phase of TSS when electron wave functions between two closed paths interfere destructively. However, the destructive interference effects are reduced with applied magnetic fields resulting in a positive MR, as observed in many metallic compounds with large spin-orbit coupling (SOC) [130].

To understand the role of scattering with temperature and magnetic field, well established Kohler's rule [130] has been applied to MR data. Kohler's law predicts that when the charge carriers acquire same scattering rate, the plot of MR ratio as a function of $[B/\rho_{xx}(0)]^{\beta}$ at different temperatures and fields should merge onto a single curve (where $\rho_{xx}(0)$ is zero-field resistivity and β is a constant) [130]. The plot between MR ratio vs. $B/\rho_{xx}(0)$ with $\beta = 1$ is shown in figure 5.2 (d). All the MR curves merge into a single line, which is in good agreement with the Kohler's law. This confirms that the transport property in the present sample is due to a single kind of charge carriers only. The little deviation of the MR curve at 300 K from the single line can be observed on the log scale (Figure 5.2 (d): bottom inset). The dominance of phonon scattering at high temperature might be the reason for this deviation [131], [132]. The variation of MR ratio (%) at 7T with mobility at different temperatures is shown in figure 5.2 (d) (top inset). A linear dependence of the MR ratio (%) on mobility can be observed from the graph.

To obtain the number of conduction channels and phase coherence length we have fitted the magnetoconductivity (MC) data with the HLN formula [23]:

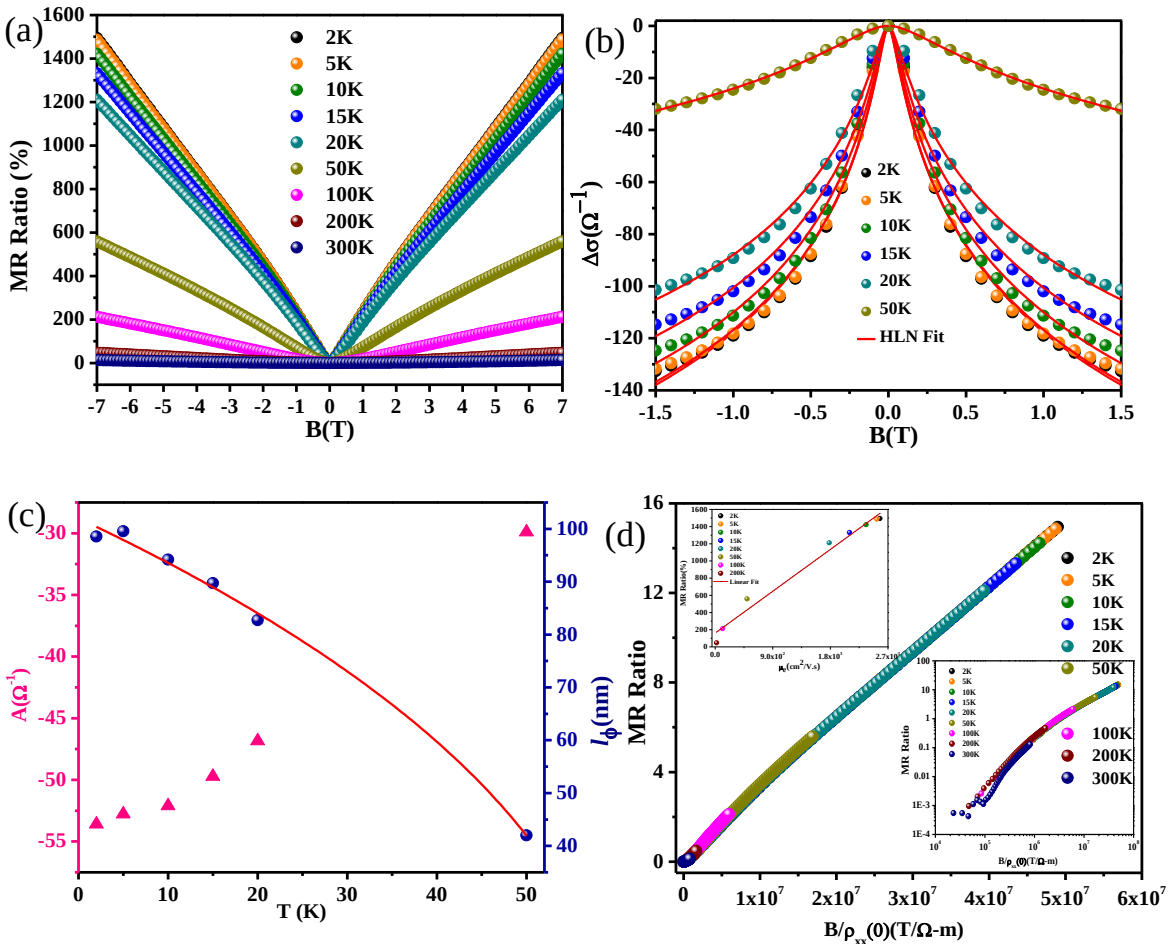

Figure 5.2: (a) Magnetoresistance ratio (%) as a function of magnetic field for $Bi_{1.9}Dy_{0.1}Te_3$ at various temperatures, (b) HLN fit on Magnetoconductivity at the low magnetic field (-1.5T to 1.5T), and at different temperatures, (c) Variation of number of conduction channels and coherence length with temperature, (d) The Kohler's plot for magnetoresistance data measured at different temperatures, Top inset: Linear variation of magnetoresistance with mobility, Bottom inset: Kohler's plot on logarithmic scale.

$$\Delta\sigma = \sigma(B) - \sigma(0) = A\left[\psi\left(\frac{1}{2} + \frac{h}{8\pi eBl_{\varphi}^2}\right) - ln\left(\frac{h}{8\pi eBl_{\varphi}^2}\right)\right], \qquad (5.1)$$

Where, $A(=\frac{\alpha e^2}{\pi h})$ represents the number of conduction channels with $\alpha = -\frac{1}{2}$ per conduction channel and ψ is digamma function, l_{φ} is the phase coherence length. Fitted MC curves with HLN formula at the low magnetic field (-1.5T to 1.5T) at different temperatures are shown in figure 5.2 (b). The obtained values of A and l_{φ} at different temperatures from HLN fitting are also shown in figure 5.2 (c). It can be noted that the obtained value of A is

almost 50 times larger than pure Bi_2Te_3 [128] suggesting the existence of large number of conduction channels as compared to pure Bi_2Te_3. To further support the WAL effect, we examined the effect of electron-electron (*e-e*), electron-phonon (*e-p*) scattering on phase coherence length (l_φ) as a function of temperature. According to the WAL effect in 3D TIs, both the '*e-e*' and '*e-p*' scattering are supposed to be emerged [133], [134]. The temperature-dependent l_φ can be described as

$$\frac{1}{l_\varphi^2(T)} = \frac{1}{l_\varphi^2(0)} + A_{ee}T^q + A_{ep}T^{q'} \quad (5.2)$$

Where, $l_\varphi(0)$ is the phase coherence length at zero temperature, $A_{ee}T^q$ and $A_{ep}T^{q'}$ are the contribution from the *e-e* and *e-p* interactions, respectively. The values of l_φ, obtained from equation (5.1) at different temperatures are fitted with equation (5.2) by fixing $q = 1$ and $q' = 2$ as shown in figure 5.2 (c). The best fit gives $l_\varphi(0)$ = 102 nm, consistent with the reports for TIs [128], [129], [135] Such a large enhancement in MR and A values in the present sample might be due to the robust surface state as compared to the pure Bi_2Te_3 [128], [136]–[139] as is also clear from the thermoelectric data (discussed below).

In order to find out the magnetic ordering, magnetic measurements were performed. The variation of magnetization (M) as a function of the magnetic field (B) at various temperatures is shown in the inset of figure 5.3. Magnetic susceptibility (χ) as a function of temperature was measured at 100 mT applied magnetic field in zero field cooled (ZFC) condition (figure 5.3) which shows that as the temperature decreases the magnetic susceptibility value increases. These experimental observations suggest the antiferromagnetic ordering in Dy doped Bi_2Te_3. Super exchange interaction between Dy^{3+} ions via Te is the probable reason of antiferromagnetic coupling [140]. Similar behavior of

magnetization with the applied magnetic field has been observed by many others in distinct magnetically ordered Bi_2Te_3 systems [123], [141]–[143].

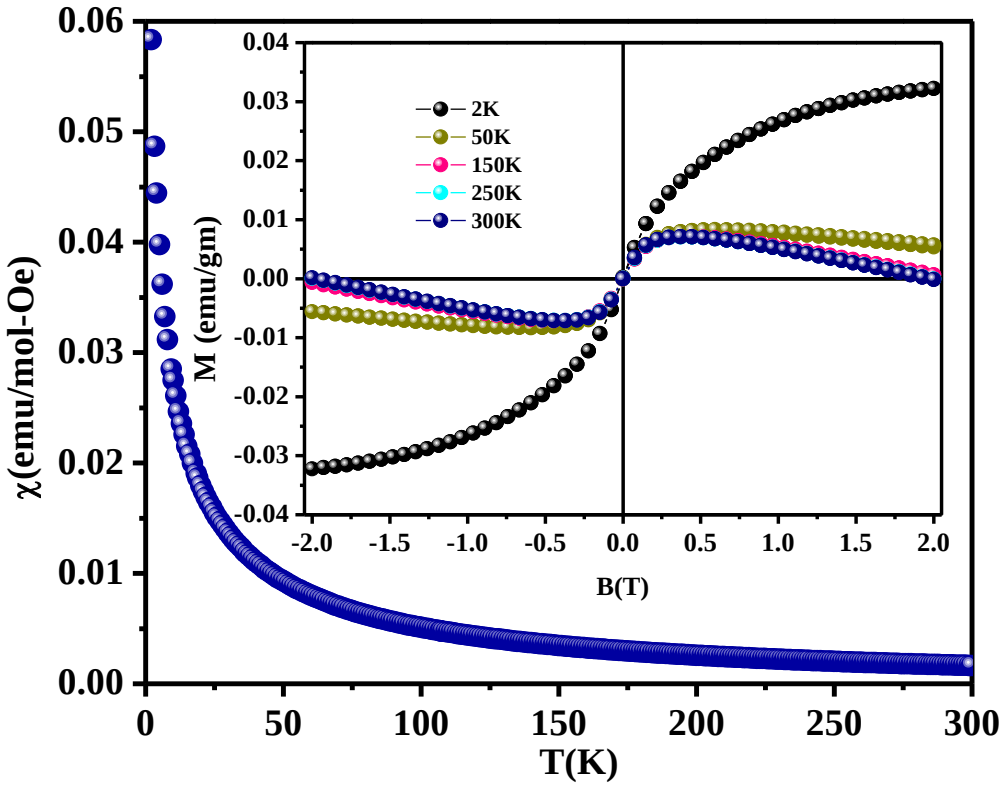

Figure 5.3: (a) Variation of magnetic susceptibility (χ) as a function of temperature measured at 100 mT applied magnetic field in zero field cooled (ZFC) condition, Inset: Field dependence of magnetization for $Bi_{1.9}Dy_{0.1}Te_3$ measured at different temperatures.

5.3.2 ARPES Study

In order to observe the electronic structure and the effect of magnetic ordering in $Bi_{1.9}Dy_{0.1}Te_3$, we have also carried out ARPES measurements. Figure 5.4 shows the electronic structure of $Bi_{1.9}Dy_{0.1}Te_3$ taken along K-Γ-K direction of the hexagonal surface Brillouin zone with s-polarized light and p-polarized light respectively. The difference between the experimental observations from s-polarized and p-polarized light is related to the spin-momentum locking of topological surface states. The 'V'- shaped, Dirac-like TSS are clearly visible confirming topological non-triviality of the electronic structure of

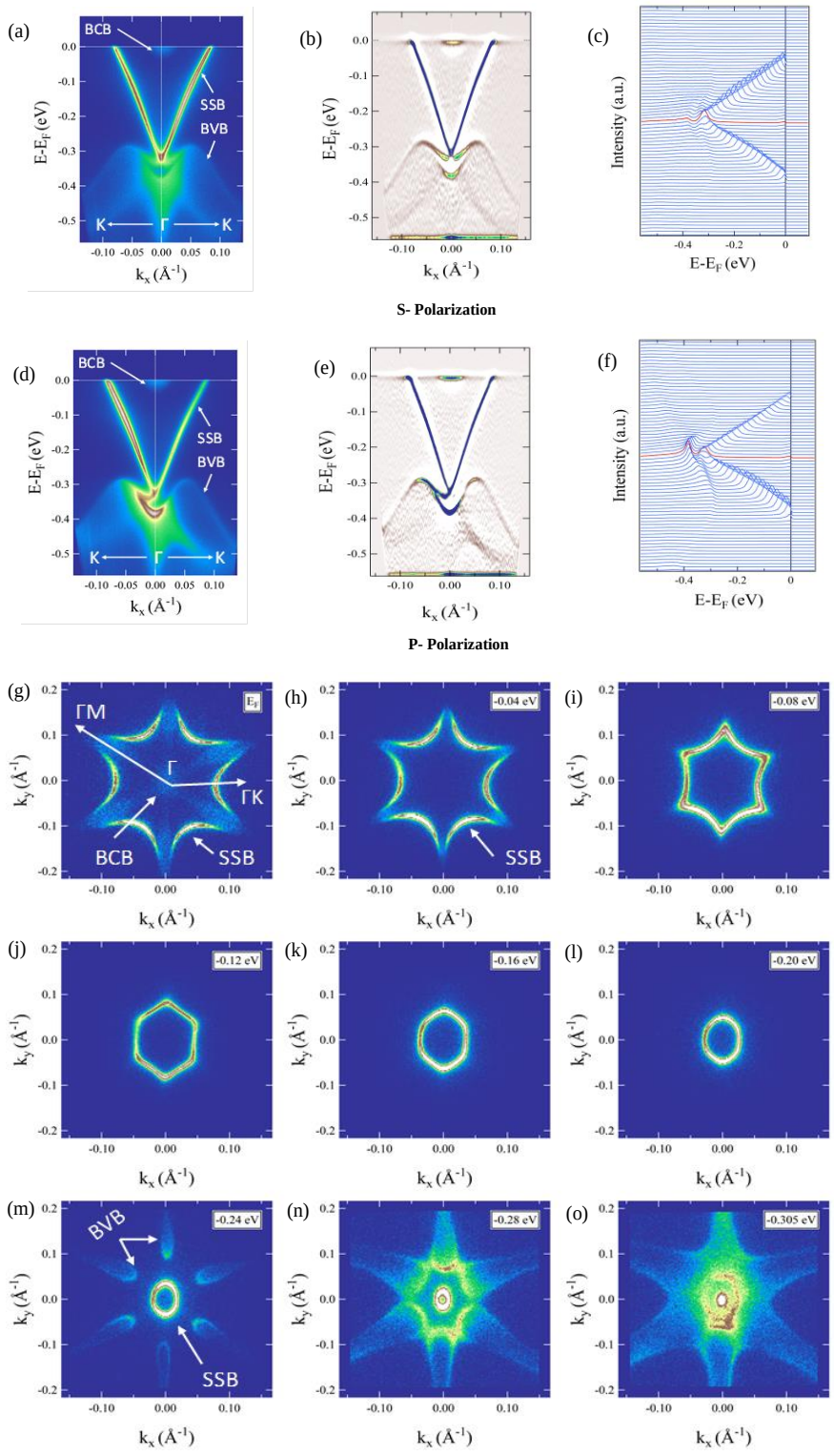

Figure 5.4: (a) Electronic spectra for $Bi_{1.9}Dy_{0.1}Te_3$ taken along K-Γ-K direction (raw) (b) second derivative (c) Energy distribution curve's (EDC's) with S-polarized light, (d) Electronic spectra for $Bi_{1.9}Dy_{0.1}Te_3$ taken along K-Γ-K direction (raw) (e) second derivative (f) Energy distribution curve's (EDC's) with P-polarized light, (g) - (o) The plots of the iso-energy contours of the ARPES spectra at different energies.

$Bi_{1.9}Dy_{0.1}Te_3$. The broad 'M'- shaped bulk valence band (BVB) is also observed at higher binding energies (BE's). The Fermi level (E_F) lies very close to the bulk conduction band (BCB) and the position of Dirac point (DP) is observed around −0.305±0.002 eV below the E_F, which lies inside the central wedge of the 'M'- shaped BVB. One can notice the ARPES intensity corresponding to the bulk conduction band (BCB) at E_F in figure 5.4 (a, b), confirming the electron-doped nature of the bulk. Consequently, *n*-type nature revealed from the ARPES measurement is consistent with Hall and thermoelectric measurements [discussed below]. Figure 5.4 illustrates two-dimensional constant energy contour plots of the ARPES intensity at different energies. On approaching the DP from the E_F, the constant energy contour plot of the TSS is changed from a hexagram to a hexagonally warped structure, then to a circle of gradually reducing radius, and then finally it shrinks to a point, the DP, as is generally observed in other TIs [30], [144]. Other than the TSS, the six-fold petal-like intensity pattern at energy -0.24 to -0.305 eV is also visible, which originates from the BVB. The obtained surface carrier density ($n=S_f/(2\pi)^2$) derived from the TSS is ($\sim 1.5 \times 10^{13}$) cm^{-2}. In figure 5.4 (c) only a single peak appears in the energy distribution curve (EDC) at the DP, which suggests the absence of appreciable gap opening at the DP [30]. Our ARPES results support that $Bi_{1.9}Dy_{0.1}Te_3$ is a gapless magnetic topological insulator.

5.3.3 Hall Effect and Thermoelectric Power

Hall resistivity (ρ_{xy}) as a function of the magnetic field (B) at different temperatures is shown in figure 5.5 (a). The negative slope of ρ_{xy} is indicating that the charge carriers are electrons. Te-vacancies and anti-site disorders could be the possible reasons behind the *n*-

type nature of the sample [145], [146]. The carrier concentration (n_e) and carrier mobility (μ_e) were evaluated from the slope of the Hall data at different temperatures and at the high

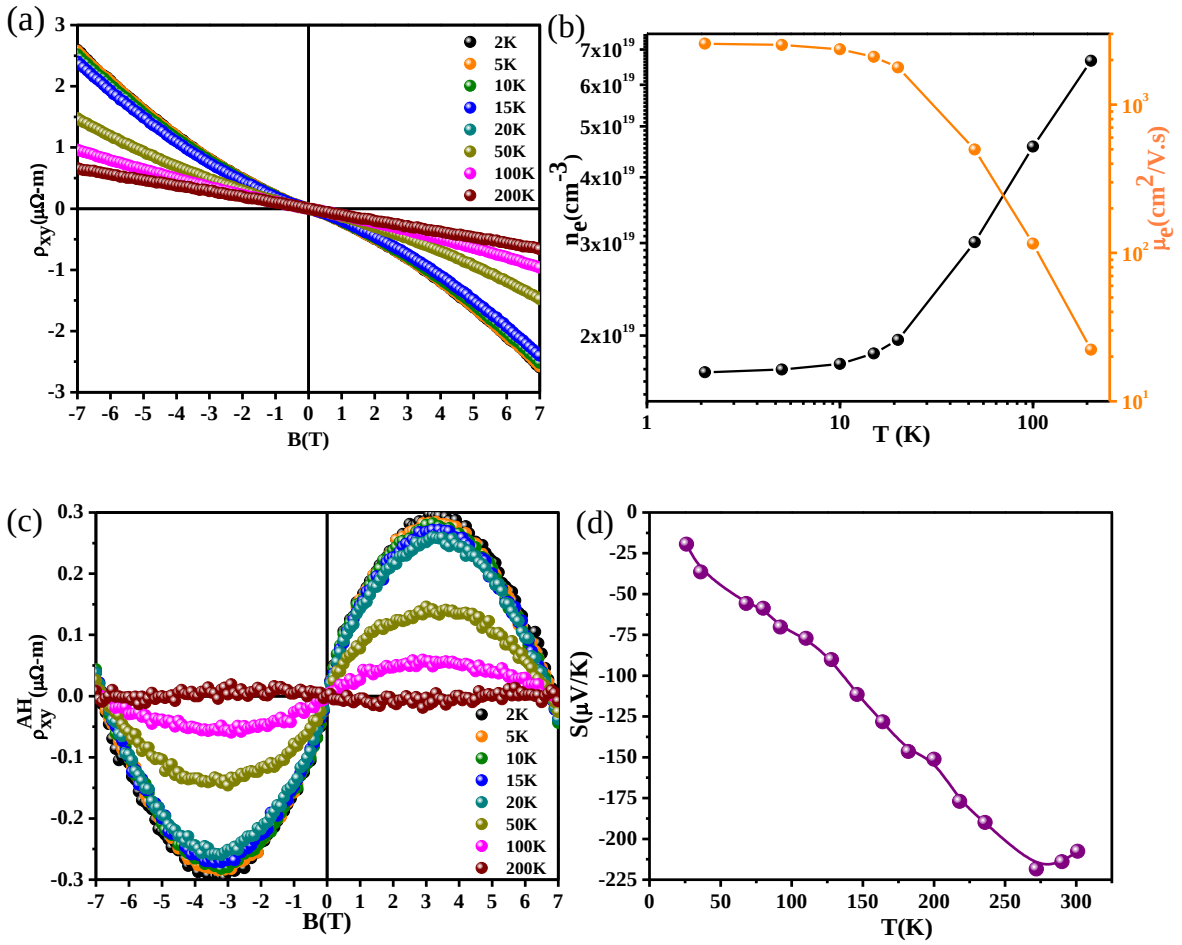

Figure 5.5: (a) Magnetic field dependence of the Hall resistivity for $Bi_{1.9}Dy_{0.1}Te_3$. (b) The variation of carrier concentration and carrier mobility as a function of temperature, (c) Anomalous Hall contribution (ρ^{AHE}) *vs.* magnetic field at different temperature. (d) Variation of Seebeck coefficient (*S*) with temperature.

magnetic field. The variation of n_e and μ_e with respect to temperature is shown in figure 5.5 (b). It can be seen from the graph that electron concentration is increasing with increasing temperature which corresponds to a decrease in mobility. The value of mobility is decreased from 2574 cm^2/Vs (2 K) to 22 cm^2/Vs (300 K). The dominance of bulk contribution at high temperature might be the reason for the enhancement in carrier density, and a decrease in mobility. Simultaneously, thermal vibration might also be a reason for the

decrease in mobility at high temperature. The value of n_e is ranging from 1.7×10^{19} cm^{-3} (2 K) to 6.7×10^{19} cm^{-3} (200 K), but for pure Bi_2Te_3 [128] the reported value varies from 6×10^{17} cm^{-3} to 3×10^{18} cm^{-3} at 2 K. It has been shown [128] that as the carrier concentration increases the MR value decreases. But in the present case even though n_e is larger than those reported, the MR is larger. Which also clearly suggests that the observed MR is due to the surface state only as the obtained n_e value is for bulk as it is determined from the Hall effect [31], [132], [147]. All the above information indicates that the enhanced MR is due to the surface state only. The robustness of the surface state can also be observed from the Seebeck coefficient (*S*) data. Figure 5.5 (d) shows the variation of the Seebeck coefficient (*S*) with temperature. The negative slope of the Seebeck coefficient reflects *n*-type nature of the sample. The negative value of *S* of $Bi_{1.9}Dy_{0.1}Te_3$ is because of the fact that E_F lies in the bulk conduction band which is confirmed by the Hall effect [figure 5.5 (a)] and angle-resolved photoemission spectroscopy (ARPES) measurements. The value of the Seebeck coefficient for Dy doped Bi_2Te_3 reaches ~218.5 μV/K at 272 K and 207 μV/K at 301 K. According to the Drude model for free electron gas, the Seebeck coefficient is expressed as

$$S = \frac{\pi^2}{6}\left[\frac{k_B T}{E_F} \times \frac{k_B}{e}\right] \tag{5.3}$$

A large carrier density, hence a large E_F could significantly reduces *S*. From the Hall effect data the obtained carrier density (discussed above) increases with temperature. Therefore, the enhanced *S* value is due to the surface contribution. This further confirms the robustness of the surface state.

Nonlinearity in Hall data can also be seen clearly at a low field and low temperature, which is diminishing with increasing temperature and almost vanishes at 200 K. Two possible reasons may be responsible for nonlinearity in Hall data. First, both electron and

hole bands are participating in electric transport, and the second one is the anomalous Hall effect (AHE). However, these two phenomena show two different temperature dependence. The contribution from hole band gets more pronounced with increasing temperature while AHE, which emerges from Berry curvature in momentum space, is reduced [148]. In the present case, the nonlinearity in Hall data is reduced with increasing temperature and almost vanishes at 200 K. Furthermore, as has already been mentioned from Koehler's plot that there exists only single charge carrier. The large negative *S* value also supports the existence of single charge carrier. Therefore, the observed nonlinearity is a clear indication of AHE. We have also estimated the value of AHE at different temperatures. The Hall resistivity of a magnetic sample can be written as, $\rho_{xy} = \rho^{O}+\rho^{AHE}$, where the first term is ordinary Hall contribution ($\rho^{O} = R_O B$, where, R_O is the ordinary Hall coefficient, B is the magnetic field) and the second term is the AHE contribution, which comes from the magnetization of the material ($\rho^{AHE} = R_{AH}M$, where R_{AH} is anomalous Hall coefficient, and M is magnetization of material). Anomalous Hall contribution can be extracted by subtracting the ordinary Hall contribution from measured Hall resistivity (ρ_{xy}). The extracted Anomalous Hall contribution (ρ^{AHE}) is positive and is shown in figure 5.5 (c). It is observed that a peak is centered around 3.5 T up to 100 K. The peak value is decreasing with increasing temperature and almost vanishes at 200 K as shown in figure 5.5 (c). Similar results have also been observed in other topologically non-trivial systems [18], [149], [150]. It is observed as the temperature increases (that is with an increase of carrier concentration) the ρ^{AHE} decreases. In a recent paper [150], the existence of both positive and negative Hall conductivity has been reported in the Mn-doped Bi_2Se_3 system. From the effect of the doping content and gating, it has been shown that with the increase of carrier

concentration the negative and positive anomalous Hall conductivities respectively decrease and increase. Consequently, it has been suggested that the negative Hall conductivity is due to the surface state and positive Hall conductivity is due to the bulk state. For the present case, the observed positive Hall conductivity increases with the n_e. Therefore, it can be considered that the observed anomalous Hall effect is due to bulk. In fact, the sign of the AH effect can be tuned by varying the chemical composition. For instance, the $(Bi,Sb)_2Te_3$ thin films doped with Cr, V, or Mn exhibit [117], [151]–[153] positive AH resistances, whereas the Mn-doped $(Bi,Sb)_2(Te,Se)_3$ has an opposite sign [154] suggesting the sign difference may be attributed to the details of the p–d exchange interactions. In the report of Gd doped Bi_2Te_3 [123] it has been inferred that the topological surface state can possibly coexist with localized magnetic impurity bands. In the present case even at room temperature, the magnetic ordering is observed and also ARPES study indicates the non-coexistence of the surface band gap. Furthermore, on the basis of the massive Dirac Fermion model [155]–[157], the total anomalous Hall (AH) conductivity in the TI surface states is given by

$$\sigma_{AH} = - (8e^2/h)(E_F\Delta^3)/(E_F + \Delta^2)^2 \qquad (5.4)$$

Where E_F is the Fermi energy and Δ is half of the energy gap. From the ARPES it is found that the 5% Dy doping does not open any gap. Therefore, eqn. (4) suggests that there is no surface effect in the σ_{AH}. Moreover, in Bi_2Te_3 the TSS exist at low temperature and in the present case, the σ_{AH} is found even at 200 K which further supports the bulk origin of σ_{AH}. This observed AHE is due to the AFM ordering as in an AFM system with broken time-reversal symmetry and spin-orbit coupling the AHE is predicted to be significant [18], [158].

5.3.4 Theoretical Analysis

To further understand the effect of Dy doping into Bi_2Te_3 on its energetics and magnetic properties, we additionally performed spin-polarized first-principles calculations within the framework of density functional theory (DFT) [159]. To fulfill the objectives, we adopt Vienna ab-initio simulation package (VASP) [160] which is based on pseudo-potential method. The semi-local functional of Perdew-Bruke-Ernzerhof generalized gradient approximation (PBE-GGA) [161] is considered as exchange-correlation functional into computations. Further, the core and valence electron interaction effects are included in the projector-augmented-wave (PAW) method into pseudopotential calculations. We have considered Dy (6s, 4f), Bi (6s, 6p) and Te (5s, 5p) electrons as valence while others are assumed as core electrons. The plane-wave basis sets are expanded by supplying kinetic energy cutoff equal to 350 eV. We set high energy convergence criteria upto 10^{-5} eV for extracting numerical data for all set of calculations. The Brillouin zone (BZ) integration for conventional cell (supercell) was performed at 8×8×8 (6×6×1) Monkhorst-Pack [162] k-points mesh by adopting conjugate gradient scheme. The residual Hellman-Feynman force on atoms reduced upto $\leq$ 0.01 eV/Å at measured lattice constants ($a = b$ = 4.386(8) Å, c = 30.499(5)). The structure optimization in the form of relaxation of the atomic position shows that the neighboring atoms of Dy move towards and accommodate with smaller Dy-Te bond length, but the atoms far from Dy shows minute change in Dy-Te bond length and maintain its crystal structure. The change in bond length between Dy-Te varied from 0.01 to 0.1 Å with respect to Bi-Te. To study the effect of dopant interaction on the magnetic behavior of material, we have considered 2×2×1 supercell ($Dy_2Bi_{22}Te_{36}$) consisting of 4 formula units. However, the electronic properties of Dy-doped system were studied for

supercell of size $2 \times 1 \times 2$ which consist total six Quintuple layers (QLs) as shown in figure 5.6 (a). For understanding surface states of considered system, we have generated ~ 15 Å vacuum in the c-direction of $2 \times 1 \times 2$ supercell. The calculation has been made by considering the spin-orbit coupling. It has been established that the use of GGA

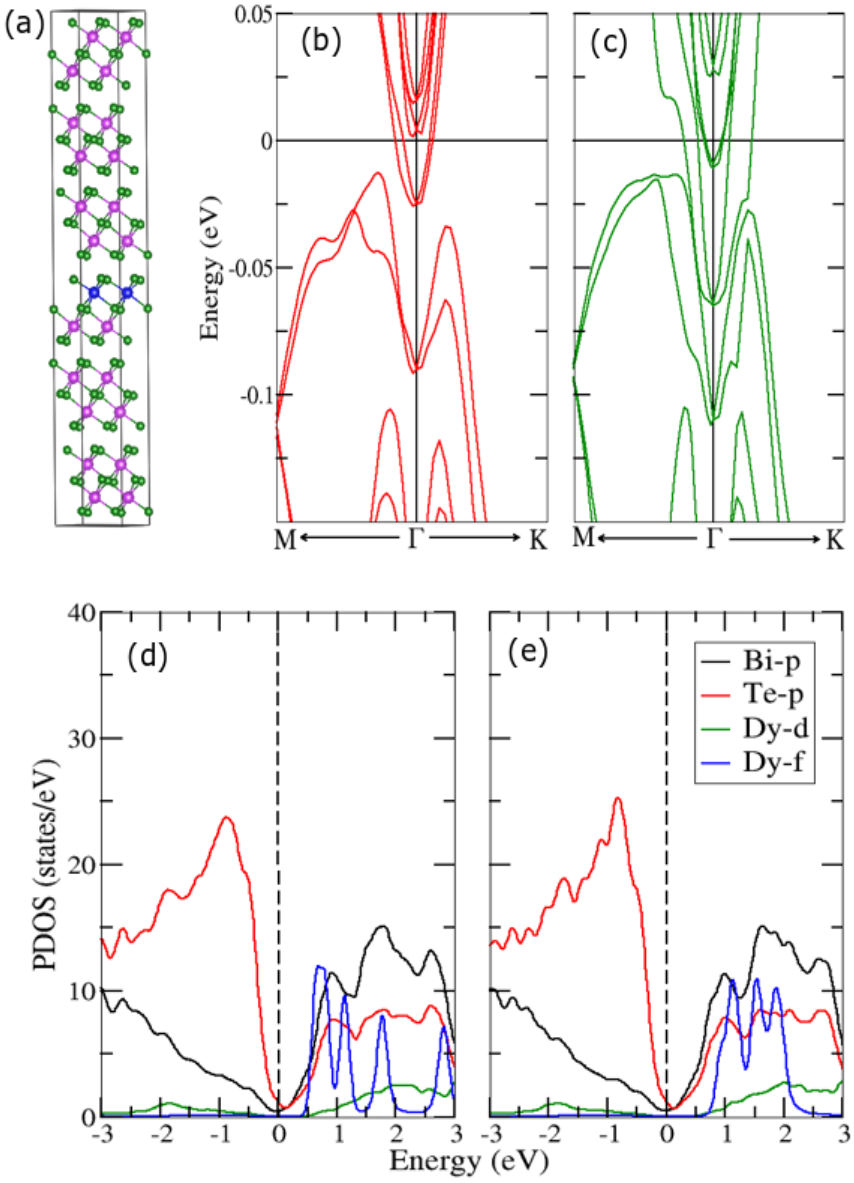

Figure 5.6: (a) The optimized crystal structure of 2×2×1 hexagonal supercell of $Dy_2Bi_{22}Te_{36}$ shows Dy (blue), Bi (magenta) and Te (green) atoms by filled solid sphere. (b) Band structure of $Dy_2Bi_{22}Te_{36}$ for bulk (red) (c) Band structure of $Dy_2Bi_{22}Te_{36}$ for surface states (green). The calculated projected density of states of Dy doped Bi_2Te_3 are presented for (d) bulk (red), and (e) surface states (green).

functional into calculation of electronic structure of a material may severely underestimate energy band gap of a material. Therefore, to overcome this difficulty we adopt GGA+U [163] approach and shifted *f* orbital of Dy by taking into consideration the Hubbard term U = 7.0 eV [164] which matches our experimental results well.

Our calculations for $Dy_2Bi_{22}Te_{36}$ confirm the existence of stable ferromagnetic (FM) and antiferromagnetic (AFM) ground states with magnetic moment (MM) ~ 4.7 μ_B/Dy. However, the total energy difference between FM and AFM configurations ($\Delta E=E_{FM} - E_{AFM}$) is 3.0 meV for the two Dy_{Bi} (at a distance of 4.38Å) located at first nearest neighbor (NN) and in same QL. We have also performed calculation when a pair of Dy_{Bi} is placed at the second NN (at a distance of 7.59 Å) in the same QL and the ΔE becomes equal to 1.0 meV. The decrease in ΔE while increasing NN distance between a pair of Dy_{Bi} confirms that the AFM coupling seems to be achieved due to a super exchange interaction (J) between Dy ions [165]. The calculated magnetic coupling strength [$(E_{AFM} - E_{FM})/2$] for two Dy atoms in the same QL and different QL at first and second nearest neighbor, respectively, has been presented in table 1. We have explored other possibilities to place Dy_{Bi} in the neighboring QL and observed that ΔE of FM and AFM states increases by more than 30 meV with same MM. Therefore, the stability of the AFM state is higher when the defect pair Dy_{Bi} is placed in the same QL.

Further, in order to unearth the underlying physics, we have also performed systematic study of electronic band structure and density of states for Dy doped Bi_2Te_3. The calculated band structure for bulk and surface states are presented in figure 5.6 (b) and figure 5.6 (c) respectively. From figure 5.6 (b) it is obvious that the separation between valence and conduction band minimum (CBM) at Γ is ~ 55 meV which supports our experimental

result. Interestingly, when looking to its surface states, the CBM shifts toward lower energy valence band and touches the valence band in the vicinity of Γ in $\Gamma - M$ direction of BZ. This feature is consistent with our ARPES data (figure 5.4) in which CBM touches the valence band in the direction of wave vector. To get deep insight for calculated electronic band structure, we now concentrate our attention in calculating contribution of hybrid orbitals by performing projected density of states (PDOS) calculations. The calculated PDOS for bulk and surface states of Dy doped Bi_2Te_3 is presented in figure 5.6 (d) and (e) respectively. Looking to PDOS for bulk system, it is clear that both valence and conduction band edges are formed by strong hybridization of Bi-p and Te-p orbitals. The contribution of Dy-*f* orbitals appears around 0.5 eV above to the Fermi energy level. In case of surface states, the hybridization between Bi-p and Te-p orbitals remain almost same as that appears in bulk system. However, the Dy-*f* orbitals shifted around 0.25 eV above to the state appears in bulk system.

Configurations (i,j)	d(Å)	$[(E_{AFM} - E_{FM})/2]$(in meV)
(0,1)	4.383	-1.55
(0,2)	6.572	-0.35
(0,3)	7.591	-0.50
(0,4)	7.893	-0.05

Table 5.1: Two Bi atoms are replaced by dopant (Dy) atoms at site i (=0) and j (j=1, 2, 3, 4) in 2x2x1 supercell of Bi_2Te_3. The magnetic coupling strength $[(E_{AFM} - E_{FM})/2]$ (in meV) between two substitutional atoms with different distances (d) in Å are also presented below. We have ignored higher neighboring configuration whose distances are greater than ~7.9 Å.

5.4 Conclusion

We have investigated the electronic structure, magnetotransport properties, Seebeck coefficient and magnetization of $Bi_{1.9}Dy_{0.1}Te_3$ topological insulator with a high residual resistivity ratio of 59. We found enhanced magnetoresistance of ~1500% at 7 Tesla. The large MR has been attributed to the robust surface state. Magnetic measurements together

with density functional theory calculation indicated the presence of an antiferromagnetic state, which is consistent with the existence of an anomalous Hall effect. The origin of magnetic ordering and AHE has been attributed to the bulk properties. By means of high-resolution ARPES, we have found that the topological surface state has no appreciable energy gap at the Dirac point, suggesting $Bi_{1.9}Dy_{0.1}Te_3$ is a gapless antiferromagnetic topological insulator. Therefore, for both the surface and bulk states the different interesting behaviors are observed indicating the potentiality of these topological insulators in applications.